Control of the California Extremely Large Telescope primary mirror

Douglas G. MacMartin, Gary A. Chanan

Douglas G. MacMartin, Gary A. Chanan, "Control of the California Extremely Large Telescope primary mirror," Proc. SPIE 4840, Future Giant Telescopes, (30 January 2003); doi: 10.1117/12.458150

SPIE.

Event: Astronomical Telescopes and Instrumentation, 2002, Waikoloa, Hawai'i, United States

Control of the California Extremely Large Telescope Primary Mirror

Douglas G. MacMartin[a] and Gary Chanan[b],

[a]California Institute of Technology
Department of Control and Dynamical Systems, Pasadena CA 91125
[b]University of California, Irvine,
Department of Physics and Astronomy, Irvine CA 92697

ABSTRACT

The current design concept for the California Extremely Large Telescope (CELT) includes 1080 segments in the primary mirror, with the out-of-plane degrees of freedom actively controlled. We construct the control matrix for this active control system, and describe its singular modes and sensor noise propagation. Data from the Keck telescopes are used to generate realistic estimates of the control system contributions to the CELT wavefront error and wavefront gradient error. Based on these estimates, control system noise will not significantly degrade either seeing-limited or diffraction-limited observations. The use of supplemental wavefront information for real-time control is therefore not necessary. We also comment briefly on control system bandwidth requirements and limitations.

Keywords: Extremely Large Telescopes, CELT, Segmented Mirror Control

1. INTRODUCTION

An initial design for the 30-meter diameter California Extremely Large Telescope (CELT) has been completed.[1] The current design for the primary mirror has 1080 hexagonal segments, as illustrated in Figure 1. The out-of-plane degrees of freedom will be actively controlled by 3240 actuators using feedback from 6204 edge sensors; the geometry is similar to that of the Keck telescopes,[2,3] but with 30 times more actuators. Previous papers[4,5] describe the preliminary design concepts for the active control hardware, and preliminary control analysis. Herein, we present an error analysis of the primary mirror active control. An analysis of control system error sources is critical in order to ensure that the telescope error budget can be met. The analysis also helps to define hardware specifications, select the control bandwidth, and assess the need for additional measurements such as wavefront sensing.

CELT will operate in two modes, seeing-limited (without adaptive optics), and diffraction-limited (with adaptive optics). The goal for seeing-limited observations is to degrade atmospheric seeing by less than 10%. We assume that the 80% enclosed-energy diameter for the atmospheric turbulence degraded image is $\theta(80) > 0.567$ arcseconds 90% of the time, thus the telescope should contribute $\theta(80) < 0.26$ arcseconds.[1] The seeing-limited error budget allocates 53 milli-arcseconds (mas) for control errors, including actuator noise, the error in desired sensor readings, sensor noise, and residual vibration above the control bandwidth. Based on estimates for the first two sources, the remaining two sources must contribute no more than 40 mas. In order to not significantly degrade adaptive optics performance, the diffraction-limited error budget is 50 nm rms of un-correctable wavefront error due to all telescope sources. Low wavenumber distortions of the primary mirror can be corrected by the adaptive optics system provided that this does not result in saturation of the AO actuators. The error budget for active control errors is 17.8 nm, leading to a requirement that the impact of sensor noise and uncontrolled frequencies need to each be less than $\sim$10 nm.

We consider two types of sensors. Capacitive edge sensors measure relative displacement between neighboring segments.[4] The Keck telescopes also use relative displacement sensors, however, the sensor design for CELT has been changed significantly. We assume that the CELT edge sensor noise will be at least as small as at Keck, and use operational data from the Keck telescopes to establish the expected noise amplitude. We also evaluate the potential for using wavefront information to supplement edge sensors for the lowest spatial-frequency modes. An initial analysis of the error propagation resulting from edge sensor noise is described by Chanan.[5] With only the capacitive edge sensors, the low wavenumber (spatially smooth) modes have poor observability, and thus have larger rms surface errors for a given sensor noise. The impact of these errors is partially mitigated because, for a given

Future Giant Telescopes, J. Roger P. Angel, Roberto Gilmozzi, Editors,
Proceedings of SPIE Vol. 4840 (2003) © 2003 SPIE · 0277-786X/03/$15.00

surface error, the poorly observable low wavenumber modes do not contribute as much to either the seeing-limited or diffraction-limited error budgets as do the higher order modes. The use of wavefront information for real-time feedback is not necessary; sufficient performance can be achieved with the edge sensors alone, while wavefront information will have higher sensor noise than the edge sensors on any time scale due to atmospheric turbulence. Wavefront information will still be required for determining the desired sensor readings.

The overall contribution to the error budget from sensor noise requires estimating three factors:

- The noise multiplier from sensor noise to errors in estimating the primary mirror shape,
- the expected sensor noise power spectral density (PSD), filtered by the control bandwidth, and
- the conversion of errors in the primary mirror shape to $\theta(80)$ (seeing-limited) and uncorrectable wavefront errors (diffraction-limited).

Each of these factors will be discussed, followed by brief discussions on the use of wavefront information for feedback (Section 5) and expected control bandwidth requirements (Section 6).

2. CONTROL ANALYSIS

2.1. Control Problem

A description of the control hardware, some definitions, and analysis are necessary for background.[1, 6]

Three actuators located at the vertices of an equilateral triangle will adjust the piston, tip, and tilt of each segment in response to a set of sensor readings, including displacement sensors and possibly wavefront sensors. There will be two displacement sensors along each inter-segment edge for a total 6204 sensors. These sensors are sensitive to both the relative out-of-plane displacement between segments, and also to changes in the dihedral angle between segments. These edge sensors redundantly measure all $(3n_{\rm seg} - 3)$ relative pistons, tips, and tilts of the segment array. A wavefront sensor has also been considered to improve the precision of estimating low spatial frequency deformations of the array.

The primary mirror deformation with respect to the desired shape is described by the displacement at each of the actuator locations, denoted by the vector x, with rms σ_x. The rms surface error of the primary mirror is $1.06\sigma_x$ (based purely on geometry), and the wavefront error is double the surface error. The contribution to enclosed energy on the sky, $\theta(80)$, depends on rms segment rotation $\theta_{\rm rms}$ rather than surface errors; for a Gaussian distribution, $\theta(80) = 1.27 \cdot 2\theta_{\rm rms}$.

The vector of sensor measurements y that result from segment displacements satisfies

$$y = Ax + \delta + n. \tag{1}$$

The matrix A is determined from the segment geometry and the actuator and sensor locations. We assume uncorrelated white sensor noise n with rms on each channel of σ_n. The desired sensor readings δ corresponding to the desired mirror shape are determined optically using an alignment camera similar to that used for Keck[7]; the control algorithm minimizes $(y-\delta)^2$. If wavefront information is also used, then y includes both sets of measurements, with the additional rows of A computed from the mapping between wavefront apertures and the segment geometry.

The singular value decomposition of the A matrix for edge sensors motivates a useful set of basis functions for representing spatial deflection shapes of the mirror. With $A = U\Sigma V^T$, Σ a diagonal matrix of singular values σ_i, and U, V unitary, then $\xi = V^T x$ or $x = V\xi$ is a useful change of basis. The columns of V will be referred to as "modes" and are a complete orthonormal set which spans the space of possible primary mirror deflections. Large singular values of A correspond to highly observable deflection shapes, with large deflections between neighboring segments for a given overall rms deflection. Small singular values correspond to low spatial wavenumber ("smooth") deflection shapes, with relatively less deflection between segments for given rms overall deflection; Figure 1 gives a visualization of both a high and low wavenumber mode. The matrix A has three singular values equal to zero, corresponding to overall rigid body deflection of the primary mirror. The least observable mode is "focus", corresponding to zero relative edge displacement between segments and equal dihedral angle between segments. This mode is observable with the current sensor geometry as discussed in the next subsection.

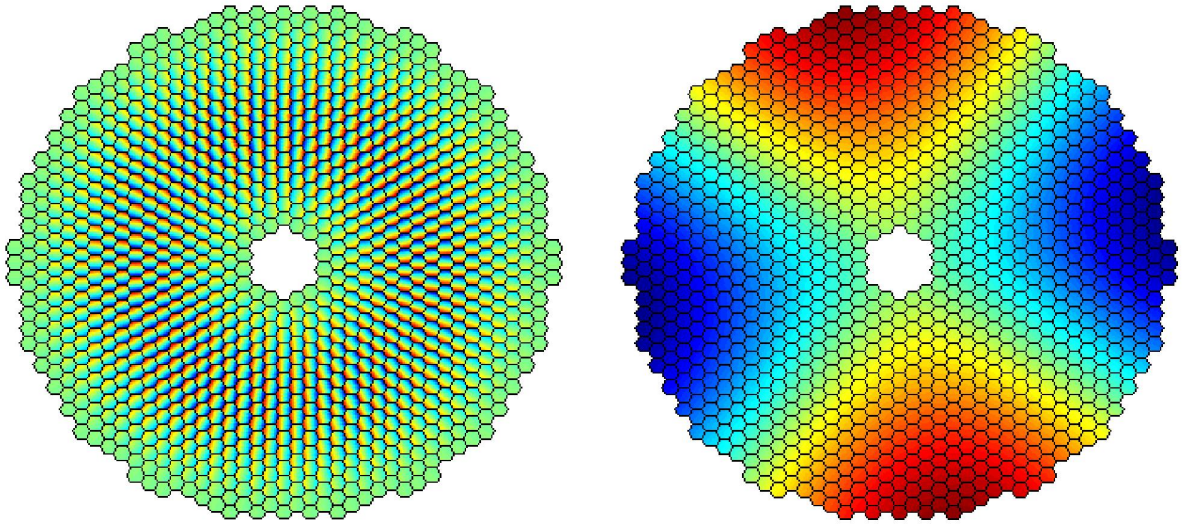

Figure 1. Two CELT primary mirror "modes", based on the singular value decomposition of A, illustrating both segment geometry and observability: most observable mode (left) and one of the least observable modes (right).

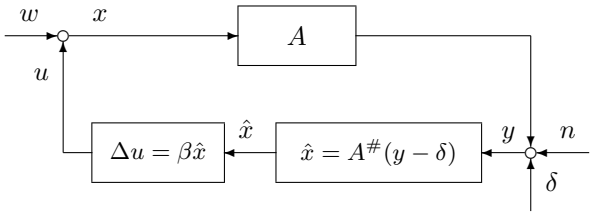

Figure 2. Control Block Diagram. Surface error x at actuator locations is the sum of the actuator command u and some disturbance w. The sensor measurement y includes a desired offset δ and noise n. The control involves estimating the displacements $\hat{x}$ and using this to determine the desired control command.

The baseline disturbance rejection control algorithm[2, 6] can be divided into two steps, shown in Figure 2. The first step is to estimate the displacements at the actuator locations given the sensor information, and the second step is to use a simple controller (integral or PI) to minimize this error.

In the absence of sensor noise the optimal estimator is

$$\hat{x} = A^{\#}(y - \delta), \tag{2}$$

where the left pseudo-inverse $(\cdot)^{\#}$ is given by

$$A^{\#} = \lim_{\rho \to 0} (A^T A + \rho I)^{-1} A^T \tag{3}$$

The left pseudo-inverse is readily computable from the singular value decomposition and has singular values σ_i^{-1} for $\sigma_i > 0$. Modes with small singular value in A have large singular values in $A^{\#}$, and hence the control law will amplify whatever sensor noise exists in these directions. Assuming white noise, then the overall noise propagation from rms sensor noise to rms errors in estimating the deflection at the actuator locations is given by $\sigma_{x-\hat{x}} = N\sigma_n$, where the noise multiplier N is

$$N = \left(\sum_{i=1}^{n_{\text{act}}} \frac{\sigma_i^{-2}}{n_{\text{act}}} \right)^{1/2} \tag{4}$$

The desired change in the actuator commands u is computed as

$$\Delta u = \beta \hat{x}, \tag{5}$$

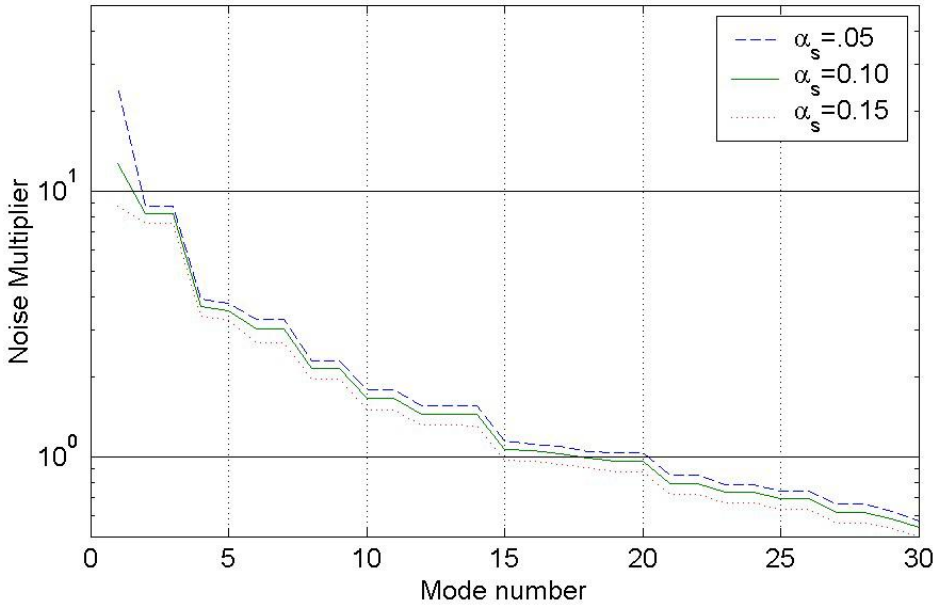

Figure 3. Noise multiplier for first 30 modes of CELT for three different sensor geometries corresponding to different ratios of dihedral to displacement sensitivity. The dependence on α_s is strongest for the first ("focus") mode.

where the gain $\beta < 1$ determines the bandwidth of this integral control law, and deflections of any spatial shape are controlled with the same bandwidth.

2.2. Noise Multiplier for CELT Edge Sensors

The CELT sensor design uses capacitor plates coated directly on the edges of the segments.[1,4] One segment has a single capacitor plate on its edge, of height b, while the neighbouring segment has two capacitor plates vertically spaced to overlap with this first plate creating two capacitors; the sensor measures the differential capacitance. This measurement is sensitive to the relative out-of-plane displacement of the two segments, since as the segments move, one capacitor will increase in area while the other decreases. The response is a function of the gap size g, hence the sensor is also sensitive to a change in the dihedral angle between the segments. A separate reading proportional to the sum of the two capacitors can be used to correct for the gain variation with changes in the gap.

If only relative displacement were sensed, then the "focus" mode would be unobservable. Because the sensor is also sensitive to dihedral, this mode is observable, and the sensitivity to other lower order modes also increases. The noise multiplier in Eq'n (4) therefore depends on the geometry. Define a dimensionless parameter, $\alpha_s = b^2/(12tg)$ that determines the relative sensitivity to dihedral angle versus displacement, where b is the height of the single capacitor on one side of the gap, $t = 255$ mm is the radius of the actuator triangle, and $g = 2$ mm is the sensor gap. The modal noise multipliers resulting from three choices of b and thus α_s are shown in Table 1 and Figure 3. For comparison, the corresponding noise multiplier for the 36-segment Keck telescopes is 4.4. The remaining analysis will be based on $\alpha_s = 0.1$.

2.3. Impact of Control Bandwidth

The resulting error in actuator positions depends on the control bandwidth (or, equivalently, the gain). The controller acts as a low-pass filter on the noise, and thus if the noise has a flat power spectral density, the resulting contribution to the error budget is proportional to the square root of the bandwidth (the variance being proportional to the bandwidth). Continuous-time analysis is sufficient if the control bandwidth is much lower than the sample rate f_s, and the resulting analysis is independent of f_s. Time delay due to sampling will alter the transfer function, but can be ignored for initial estimates.

α_s:	0.05	0.1	0.15
b:	17.5mm	24.7mm	30.3mm
Mode #	Multiplier	Multiplier	Multiplier
1	24.656	12.694	8.764
2	8.774	8.198	7.541
3	8.774	8.198	7.541
4	3.908	3.656	3.360
5	3.761	3.531	3.252
6	3.287	3.014	2.685
7	3.287	3.014	2.685
8	2.296	2.145	1.964
9	2.296	2.145	1.964
10	1.780	1.657	1.500
⋮	⋮	⋮	⋮
rms	29.3	19.5	16.1
rms w/o focus	15.8	14.8	13.5

Table 1. Noise Multipliers for CELT for different edge sensor geometry (specified by α_s or b). Only "focus" (mode 1) is strongly influenced by the geometry.

The integral control law from y to u is $A^{\#} \cdot (k/s)$, where s is the Laplace variable and $k = f_s\beta$ is the equivalent continuous-time gain. The response from disturbances to the surface error x resulting from this is $s/(s+k)$; as desired, the control law attenuates disturbances below the control bandwidth, set by k. The response from sensor noise to surface error x is the product of $A^{\#}$ and the low-pass filter $(s/k+1)^{-1}$; the filter passes estimation errors due to sensor noise through to surface errors below the control bandwidth and attenuates higher frequency errors.

The total error propagation is thus the product of the noise multiplier for $A^{\#}$ and a factor due to the low-pass filter, derived as follows. If a signal with uniform PSD Φ (variance per Hertz) is passed through a first order low-pass filter $G(j\omega)$ with corner frequency $f_0 = k/(2\pi)$ in Hertz, then the variance of the output of the filter is given by

$$\int_0^\infty G^* \Phi G \, \mathrm{d}f = \frac{\pi}{2} f_0 \Phi \tag{6}$$

The factor of $\pi/2$ results from the contribution to the output variance due to noise that is above the control bandwidth.

Two plausible control bandwidths will be considered in the following. The bandwidth sufficient to compensate for gravity and thermal deformations is the same as that in use at Keck of ∼0.05 Hz. A higher bandwidth of 1 Hz would be required to compensate for wind-induced deformation of the primary mirror; this assumption will be discussed briefly in Section 6. Note that the wind-induced deformations change more slowly for low order than for high order modes. Choosing the control bandwidth as a function of spatial frequency would minimize unnecessary errors due to sensor noise; this improvement is not taken into account in our error analysis for the higher bandwidth.

3. ANALYSIS OF KECK DATA

Data collected at the Keck telescopes has been analyzed to estimate the achievable noise with capacitive edge sensors. A total of 83 data sets were used in the analysis, 36 from Keck 1 and 47 from Keck 2. All of the data was collected between March and June 2001. Sensor readings were recorded at 100 Hz for all 168 sensors, and each data set was 10.24 seconds.

The key to interpretation of the Keck data is separating "Physical" (segment motion) from "Non-physical" (e.g. electrical noise) sensor responses. There are 168 sensor measurements, and if the motion is constrained to rigid body motion of the 36 segments of the primary mirror, then there are only 105 degrees of freedom (overall tip, tilt, and piston do not produce any inter-segment motion). The sensor set is thus over-determined.

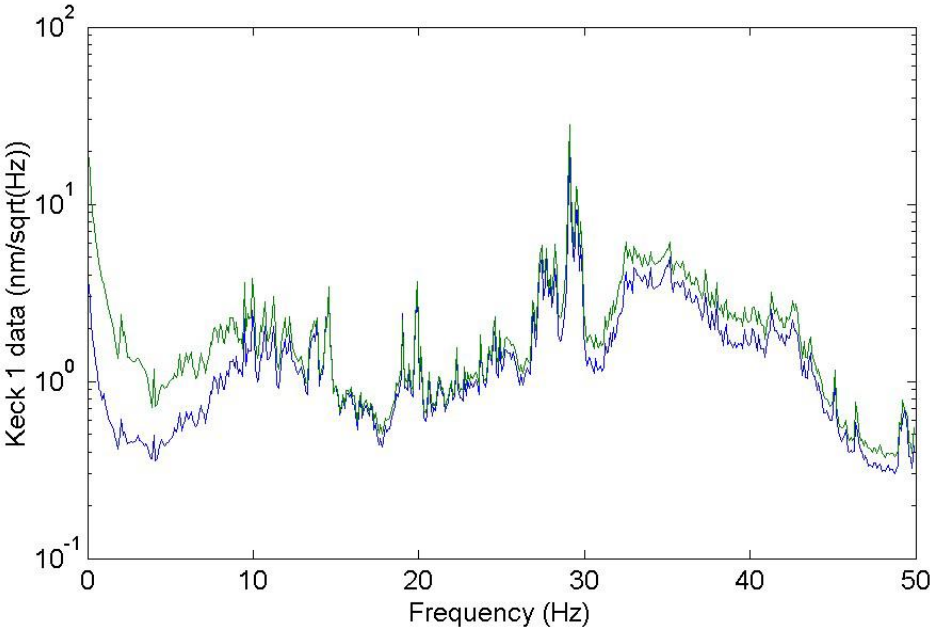

Figure 4. Average spectrum from Keck 1 edge sensors, plotted in "physical" (red, upper curve) and "non-physical" (blue) components.

Assume that the sensor measurements result from both physical motion d and sensor noise n, then $y = Ad+\delta+n$, using the Keck A matrix. Transform this measurement into two sub-spaces y_p and y_u given by:

$$y_p = (AA^{\#})(y-\delta), \tag{7}$$
$$y_u = (I-AA^{\#})(y-\delta). \tag{8}$$

Using the singular value decomposition of $A = U\Sigma V^T$,

$$AA^{\#} = U\begin{bmatrix} I_{105} & 0 \\ 0 & 0 \end{bmatrix}U^T \tag{9}$$
$$I-AA^{\#} = U\begin{bmatrix} 0 & 0 \\ 0 & I_{63} \end{bmatrix}U^T \tag{10}$$

The rank of the transformations used are thus $n_p = 105$ and $n_u = 63$; denote by $\langle y^2_{p,u}\rangle$ the sum of squares normalized by n_p and n_u appropriately. If the A-matrix used in creating these sub-spaces is exact, then y_u contains information only about the sensor noise n, while y_p is influenced by both physical motion and sensor noise. If n is uncorrelated between sensors, then the contribution of sensor noise in y_p can be estimated from the noise in y_u: we have $\langle y_u^2\rangle = \sigma_n^2$, and $\langle y_p^2\rangle = \sigma_n^2 + \langle (Ad)^2\rangle$. If the sensor noise is correlated, then this result is not true; e.g. if there is a component of sensor noise that is correlated across all sensors, then this will show up in y_p (as focus) but not in y_u.

The spectra of y_p and y_u were computed, averaged over sensors using n_p and n_u for normalization, and averaged over data sets for both Keck 1 and Keck 2. The results are plotted in Figure 4 for Keck 1; the data for Keck 2 are similar, with slightly higher levels of both physical and non-physical response. Over much of the frequency range, the "Physical" and "Non-physical" components are comparable, indicating that most of the energy in the sensor signals is due to uncorrelated noise. However, the physical component exceeds the non-physical both at low frequencies, and in the range from 25 to 45 Hz. While much of the spectrum is relatively constant from data set to data set, the amplitude of the low frequency component below 10 Hz varies considerably between data sets. This component probably results from wind-induced deformations.

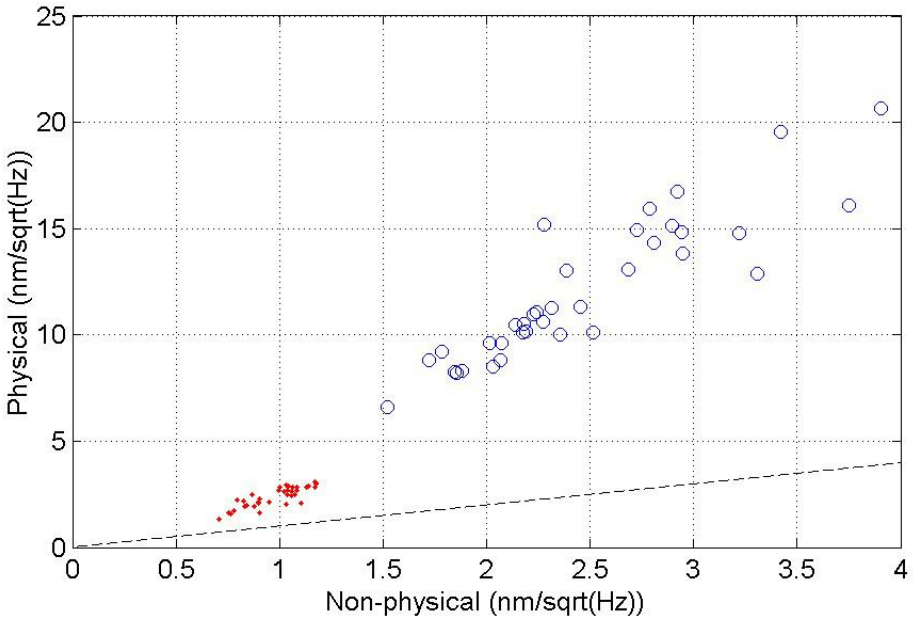

Figure 5. Low-frequency energy in physical and non-physical directions, Keck 1. Circles are 0–2.5 Hz, dots are 2.5–5 Hz. The dashed line corresponds to equal covariance. The slope of the best fit line is $\alpha^{-1} \sim 6$.

The low frequency spectrum is of primary interest to assessing control system noise, but some further analysis is required to estimate the sensor noise level. If the A matrix used in the transformation does not match the true A matrix exactly, then some physical motion will result in non-physical sensor readings, hence $\langle y_u^2 \rangle = \sigma_n^2 + \alpha \langle (Ad)^2 \rangle$ for some constant α that is a function only of the errors in the A matrix. Assuming that the A matrix is close to reality, then $\alpha \ll 1$. However, the transformation is very sensitive to small errors; a 1% random error in each non-zero element of A yields $\alpha \sim 0.2$. Figure 5 shows the correlation between the low frequency energy in the physical and non-physical components for Keck 1, averaged over 0 to 2.5 Hz, and from 2.5 to 5 Hz. Pure sensor noise should result in $\langle y_p^2 \rangle = \langle y_u^2 \rangle$, shown in the plot as a dashed line. It is clear that both the energy in the assumed physical and non-physical directions varies from data-set to data-set in a correlated fashion, but with slope neither unity (variation in sensor noise only) nor infinite (variation in physical motion only with perfect transformation). Assuming that this behaviour is a result of using an inexact A matrix to transform the motion, we conclude that the true sensor noise is the intercept where $\langle y_p^2 \rangle = \langle y_u^2 \rangle$, given by rms noise of 0.5 $\frac{\text{nm}}{\sqrt{\text{Hz}}}$. The increase above this noise level in the non-physical direction for many of the data sets is simply the result of an inaccurate transformation from sensor measurements to physical and non-physical coordinates (corresponding to errors of less than 1% between the actual and assumed A matrices). A similar plot can be generated for Keck 2. For most of the data sets, the same conclusion can be reached, that the actual noise level below 5 Hz is roughly 0.5 $\frac{\text{nm}}{\sqrt{\text{Hz}}}$, however, some of the data sets appear to indicate higher noise levels on Keck 2. Despite the change in sensor geometry from Keck, the noise levels for CELT are expected to be comparable. To be conservative, the remainder of the analysis will be conducted with double the expected noise level, of 1 $\frac{\text{nm}}{\sqrt{\text{Hz}}}$.

Although it is not directly related to the question of sensor noise propagation, a further understanding of the physical vibration at low frequencies is clearly of interest as it is relevant to the question of what needs to be controlled. Figure 6 shows the breakdown of the low frequency energy below 2.5 Hz (predominantly below 1 Hz) by mode number for one data set on Keck 1 for which the low frequency physical energy is significant; different data sets show similar trends. Also shown is the energy that would show up in each mode due only to the sensor noise n. The increase in response above the background sensor noise level is broadly distributed over all but the first few, spatially smooth modes (the content in these modes is difficult to distinguish from sensor noise due to the large noise multipliers). For this data set, the integrated contribution is at least 85 nm rms surface error, other data sets show more than 110 nm of surface error, with a mean over all data sets of 46 nm. All of these estimates neglect the

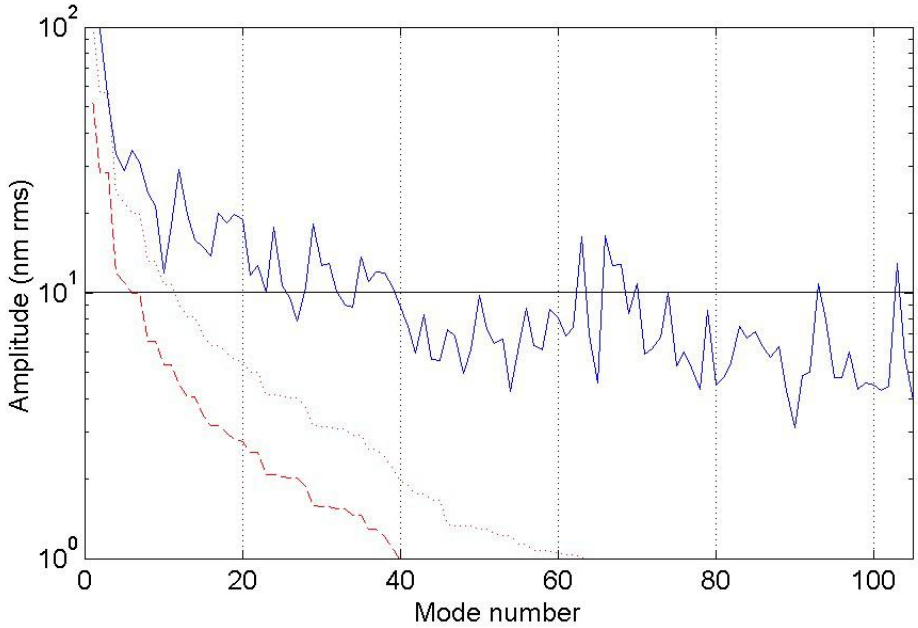

Figure 6. Distribution of low frequency energy by mode number (increasing wavenumber) for one data set from Keck 1. The fraction predictable by sensor noise is also shown (dashed), and for double the expected sensor noise (dotted).

uncertain contribution from the first 10 modes; including this increases the estimates by roughly 50%. The source of this low frequency physical vibration is partially correlated over distances larger than a segment. The amplitude, spectrum, and the fact that the amplitude varies from data set to data set are all consistent with what one might expect from wind vibration.

There is also physical vibration evident in the range 25–45 Hz. A similar analysis in this frequency range indicates that the increase in response above the background sensor noise level is predominantly in the highest ∼45 modes, indicating that the energy is due to independent segment vibrations rather than motion correlated over the mirror. The integrated contribution is typically 20–30 nm. The segment support resonance frequencies are in this band, and this vibration is likely apparent due to the excitation of these resonances.

4. ERROR BUDGET CONTRIBUTION FROM EDGE SENSORS

4.1. Surface errors

For Keck, with a control bandwidth of roughly 0.05 Hz, the rms surface error that results from sensor noise can be obtained as the product of the sensor noise, the error multiplier from the A matrix, and a factor accounting for the control bandwidth:

$$\sigma_{\rm rms} = \left(1\frac{\rm nm}{\sqrt{\rm Hz}}\right) \cdot \left(4.4\frac{\rm nm}{\rm nm}\right) \cdot \left(\frac{\pi}{2} \cdot 0.05{\rm Hz}\right)^{1/2} \simeq 1 \text{ nm}$$

This is significantly less than the rms surface error resulting from uncontrolled vibrations.

For CELT, the rms surface error due to sensor noise (using the error multipliers for $\alpha_s = 0.10$) is

$$\sigma_{\rm rms} = \left(1\frac{\rm nm}{\sqrt{\rm Hz}}\right) \cdot \left(19.5\frac{\rm nm}{\rm nm}\right) \cdot \left(\frac{\pi}{2} f_0\right)^{1/2}$$

For the same control bandwidth as Keck this gives ∼5.5 nm rms surface error, while for a 1 Hz bandwidth sufficient to compensate for some wind-induced deformation of the primary mirror, the contribution is about 25 nm. Of this, the error in focus mode is 3.5 or 16 nm for the two bandwidths, dependent on geometry, while the remaining modes would have an error of 5 or 20 nm.

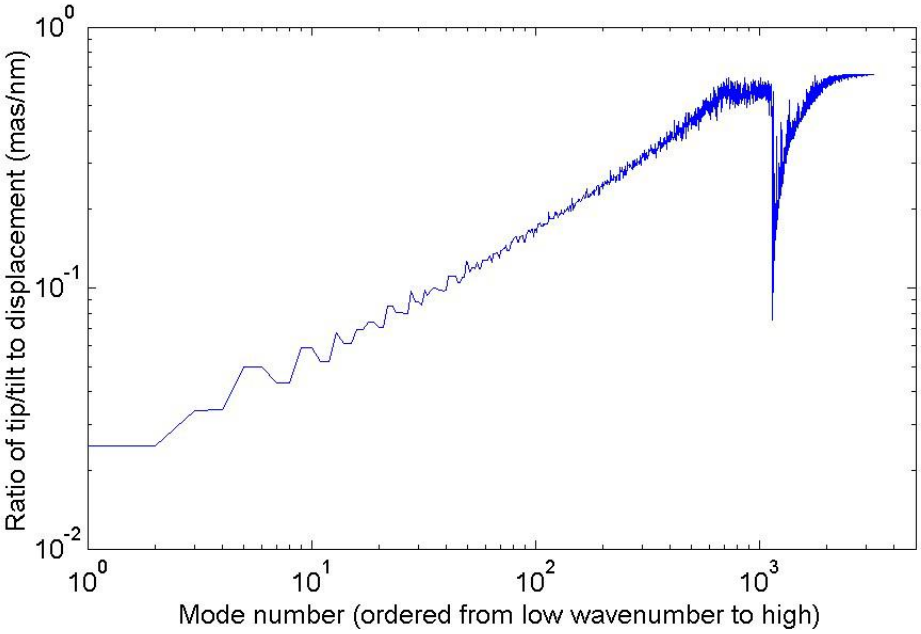

Figure 7. Ratio of rms tip/tilt of each mode to the rms displacement of each mode, in mas/nm. The low wavenumber, spatially smooth modes, have less rotation than piston. The last ∼2000 modes involve individual segment rotations and are different in character.

Focus mode differs from higher order modes in that this error can be compensated by motion of the secondary. There is a remaining error due to scalloping that is less than the error predicted above.[1] The contribution from focus mode thus depends on both the control bandwidth of the primary mirror, and that of the secondary. In the current analysis, we ignore the reduction in error that could thus be achieved. With a deformable secondary mirror, similar corrections could be applied for higher order modes as well.

The resulting contribution to the error budget requires that the rms surface error be converted into contributions to $\theta(80)$ or uncorrectable wavefront error.

4.2. Seeing-limited errors

The contribution to image blur is obtained by considering the rms segment rotation for each mode. Denote the rms noise on the i^{th} mode by ζ_i. Then $\zeta_i = \mu\sigma_i^{-1}$, where μ is a constant that depends on the sensor noise and control bandwidth, and σ_i is the corresponding singular value of the A matrix. If the noise on each individual sensor is uncorrelated, then the noise on each mode is also uncorrelated. The image blur depends on the rms rotation, not on the rms displacement error x. For each mode, compute the geometric multiplier R as the ratio of rms rotation resulting from unit displacement in that mode. The multiplier R is shown in Figure 7. The high wavenumber modes result in larger rms rotation than the low wavenumber modes. (Note that the dip past mode 1000 is not an error. The first ∼1080 modes are "smooth" with small edge discontinuities (and σ_i) that increase with wavenumber. The remaining 2000 modes involve individual segment motions.)

The mean-square rotation due to the noise ζ_i on each mode is therefore $\mu\sum((R_i/\sigma_i)/n_{\text{seg}})^2$; this factor is plotted in Figure 8. Combining the modal error multiplier with the modal rotation yields an error multiplier for CELT edge sensors of roughly 1.4 mas/nm. This is the noise propagation factor from sensor noise to estimation errors in segment rotations, analogous to the earlier noise propagation from sensor noise to estimation errors in segment displacements. To obtain the contribution to the error budget, this factor needs to be combined with the sensor noise, control bandwidth, and the conversion factor from segment tips and tilts to $\theta(80)$ of 2×1.27:

$$\theta(80) = 2 \cdot 1.27 \cdot \left(1.4\frac{\text{mas}}{\text{nm}}\right) \cdot \left(1\frac{\text{nm}}{\sqrt{\text{Hz}}}\right) \cdot \left(\frac{\pi}{2} f_0\right)^{1/2}$$

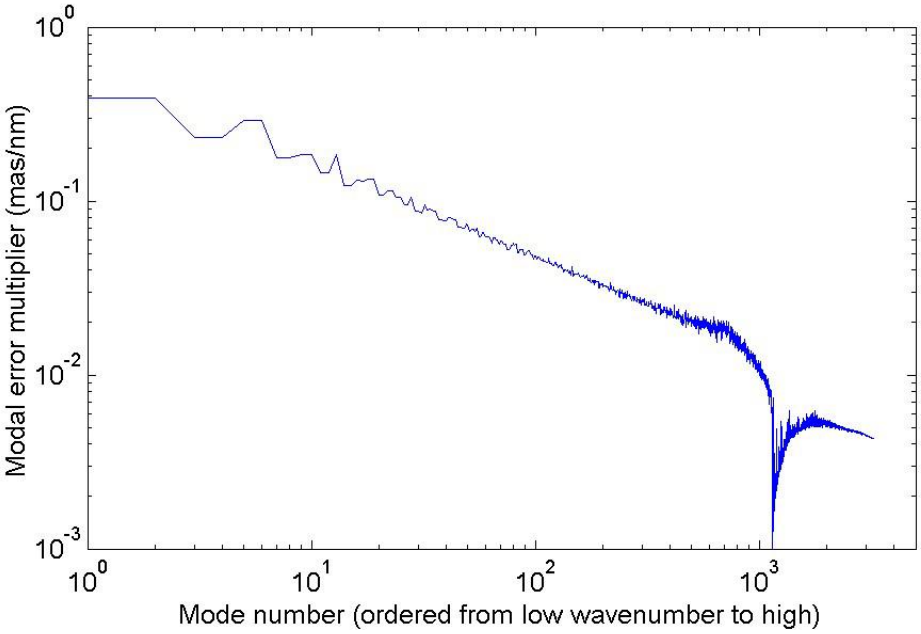

Figure 8. Modal error multipliers for seeing-limited case with edge sensors, in mas of segment rotation per nm of edge sensor noise.

With edge sensors, the two bandwidths (0.05 Hz or 1 Hz) result in $\theta(80)\sim$1 or 5 mas respectively, well below the desired target.

4.3. Diffraction-limited errors

With adaptive optics on, most of the errors introduced by sensor noise can be corrected. The errors that remain result from edge discontinuities between segments, unless there is a deformable mirror with conjugate segments. A rough estimate for these can be obtained by noting that each inter-segment edge has two edge sensors, so that the resulting uncertainty in the edge discontinuity is $1/\sqrt{2}$ times the individual sensor noise.

The fraction of the rms edge discontinuity remaining after correction by adaptive optics is approximated by a 2-dimensional geometric argument. If the DM slopes were piecewise constant, then the residual displacement can be obtained from the ratio $\eta = \ell/L$ where ℓ is the length between deformable mirror actuators and L is the segment length. Integrating the error from the best fit gives the AO controlled rms surface error $\sigma_{\rm ctrl}$ in terms of the primary mirror rms edge discontinuity $\sigma_{\rm edge}$ as $\sigma_{\rm ctrl} = (\eta/12)^{1/2}\sigma_{\rm edge}$ For a deformable mirror with $\sim$7000 actuators and a primary mirror with 1080 segments, $\eta \sim 0.4$ hence $\sigma_{\rm ctrl} \simeq 0.18\sigma_{\rm edge}$.

The residual wavefront error resulting from sensor noise propagation is therefore given by the product of all of these factors:

$$\sigma_{\rm wf} = 2 \cdot \left(0.18 \frac{\text{nm ctrl}}{\text{nm edge}}\right) \left(1 \frac{\text{nm}}{\sqrt{\text{Hz}}}\right) \cdot \left(\frac{1}{\sqrt{2}}\right) \left(\frac{\pi}{2} f_0\right)^{1/2}$$

Thus for control bandwidths of 0.05 or 1 Hz, the wavefront error will be < 0.1 nm or $\sim$0.3 nm. Thus, sensor noise propagation is not a critical issue for diffraction-limited observations.

5. INCLUSION OF WAVEFRONT INFORMATION

The analysis above indicates that edge sensors alone can be expected to provide sufficiently accurate displacement estimates for the lowest order modes, and that this conclusion also holds if either the sensor noise or the required control bandwidth are increased substantially. Nonetheless, a comment regarding the use of wavefront information for estimating the displacement of the low wavenumber modes is relevant.

With adaptive optics on, wavefront information is already being used in the control loop. The lowest frequency content of the AO deformable mirror corrections could be off-loaded to the primary mirror if desired. The need for supplemental wavefront information must therefore be asked in the context of seeing-limited observations only.

For seeing-limited observations, atmospheric turbulence in the direction of the guide star will be uncorrelated with the turbulence over most of the field of view, and is therefore "noise" on the intended measurement of the primary mirror shape. This is the dominant source of sensor noise, photon and read noise can be neglected.

Padin has estimated the contribution from atmospheric turbulence to sensor noise as a function of Zernike radial degree n and integration time. To obtain a quantifiable comparison with edge sensors, choose reasonable values for the relevant parameters: primary mirror radius $R = 15$ m, wavelength $\lambda = 1\,\mu$m, seeing $r_0 = 0.4$ m, outer scale $L_0 = 10R$, and turbulent layer wind speed $v = 10$ m/s. With these parameters, the total atmospheric phase error for $n = 2$ (focus and astigmatism) is $\sim 2\,\mu$m. Even for integration times of several seconds, the residual atmospheric phase on time scales longer than the integration time is of order 1μm. The corresponding wavefront error in $n = 2$ using edge sensors with a 1 second integration time is roughly 35 nm, or roughly a factor of 30 more accurate. While wavefront information will be required to establish the desired sensor readings δ, it will not be useful for real-time control unless the internal sensors are significantly worse than expected, or the number of segments is increased significantly (increasing the error multiplier for A).

6. CONTROL BANDWIDTH REQUIREMENTS

The previous analysis considered a 1 Hz bandwidth for the control system. Neither the requirements nor the limitations on the bandwidth have yet been addressed in detail; this section considers only preliminary estimates for both. The primary mirror active control system at the Keck telescopes has a bandwidth of ∼0.05 Hz; this is sufficient to compensate for gravity and thermal deformations. Detailed analysis of wind-induced vibration on CELT is not complete, but it is plausible that the vibration amplitudes will scale adversely with telescope size. A higher control bandwidth may therefore be required on CELT to compensate for wind-induced vibration. The higher frequency vibrations evident in Figure 4 above 25 Hz result from segment support resonances. Mitigating the corresponding resonances for CELT has not been considered, and would likely require passive damping.

The 1 Hz bandwidth estimate is based on limited analysis and data regarding wind-induced vibration. There are three sources we consider: a comprehensive data set collected at Gemini south,[8] analysis (e.g. Padin[9]), and the data analyzed herein from Keck. The Gemini data set includes wind speed measured outside the dome and at the secondary and primary, and pressure measurements distributed over the primary, for a variety of dome orientations relative to the external wind. With the dome vents closed, the wind speed at the primary is typically around 7% of external wind speed. Pressure spectra corner frequencies are typically <0.1 Hz, likely determined by the scale size of the primary mirror, with over 90% of energy below 1 Hz. Padin assumes that the outer scale of the wind turbulence on the telescope primary mirror is determined by the mirror radius. Assume a wind speed over the primary of 10% of the external wind speed (with the increased fraction relative to Gemini to account for the larger ratio of dome opening to dome diameter) then primary mirror wind speeds may be ∼1.5 m/s, giving a corner frequency of ∼0.05 Hz for the lowest modes, increasing with decreasing spatial scale. The wind crossing time for a segment would be ∼2/3 s. Finally, the low frequency vibration at Keck that is inferred by the analysis presented in Figure 4 indicates that 95% of the energy is below 1 Hz. Increasing the size of the telescope will increase the time constants. If primary mirror active control is used to compensate for wind-induced vibration, then a bandwidth on the order of 1 Hz would likely be sufficient, with higher bandwidth for high spatial wavenumber modes, and lower bandwidth for the lower modes.

Increasing the bandwidth increases errors due to sensor noise, however this will not be the limiting factor. Note from Figure 4 that the vibrations exceed sensor noise at Keck even at 10 Hz. A greater concern is control-structure-interaction (CSI). The lowest structural mode of CELT is estimated to be ∼1.2–1.6 Hz,[1] but does not involve significant mirror cell deformation; the lowest structural modes that have the potential for significant coupling with the control will be at least several Hz. Control of the highest wavenumber deflection shapes of the primary mirror surface are not likely to couple strongly to these first few structural modes and thus the achievable bandwidth for these deflection shapes may be higher than a few Hz, while the achievable bandwidth for the lowest wavenumbers may be limited to less than 1 Hz. A full assessment will require further analysis.

A control bandwidth dependent on the spatial scale is easily obtainable using either a weighted least squares estimator or a Kalman filter. This allows for improved control over the small scale deformations that contribute most significantly to the error budget, while limiting the control gain for large scale deformations both to limit the control-structure-interaction and to limit propagation of sensor noise. Therefore, even with significantly higher sensor noise than predicted herein, minimal error propagation can be maintained by using a Kalman filter to tune the control bandwidth appropriately depending on the signal to noise for each mode.

7. CONCLUSIONS

One of the contributions to the error budget of CELT associated with the active control system is the propagation of sensor noise. A detailed analysis of data collected at Keck Observatory suggests that the displacement edge sensors in use there have less than 1 $\frac{\text{nm}}{\sqrt{\text{Hz}}}$ noise. This is considerably lower than previous estimates, which did not distinguish sensor noise from low frequency segment vibration. The actuator position errors that result from sensor noise are a product of two factors; a noise multiplier computed from the sensor/actuator influence matrix, and the sensor noise filtered by the control bandwidth. The resulting wavefront error is primarily in the lowest wavenumber, spatially smooth modes. The contribution to the error budget for either seeing-limited or diffraction-limited observations is therefore less significant than implied by the surface error. For a bandwidth of 1 Hz, we expect contributions of $\theta(80)$ <5 mas in seeing-limited, and uncorrectable rms wavefront error <1 nm for diffraction-limited observations. We therefore conclude that control system errors due to edge sensor noise is not a problem for 30m class telescopes. This conclusion is dependent on the assumption that the edge sensor noise is not significantly worse than that found at Keck, and for reasonable control bandwidths. As a result, wavefront information is not required for real-time control, but only for establishing the desired sensor readings.

The bandwidth requirements and limitations for the CELT primary mirror active control system have not yet been analyzed in detail, but it is reasonable to expect that a bandwidth higher than that at Keck will be required in order to compensate for increased wind-induced vibration. Preliminary estimates suggest that a significant reduction in wind-induced vibration could be obtained with a modest bandwidth of ∼1 Hz, dependent on spatial frequency. The achievable bandwidth will be limited by control structure interaction, and not by the propagation of sensor noise.

REFERENCES

1. Nelson, J., and T. Mast, eds., *Conceptual Design for a 30-meter Telescope*, No. 34, CELT, 2002.
2. Jared, R. C. *et al.*, "The W. M. Keck Telescope segmented primary mirror active control system," *SPIE* **1236** *Advanced Technology Optical Telescopes IV*, 1990, pp. 996–1008.
3. Cohen, R., Mast, T., and Nelson, J., "Performance of the W. M. Keck Telescope Active Mirror Control System," *SPIE* **2199**, 1994, pp. 105–116.
4. Mast, T. and Nelson, J., "Segmented Mirror Control System Hardware for CELT," *SPIE* **4003**, 2000.
5. Chanan, G., Nelson, J., Ohara, C., and Sirko, E., "Design Issues for the Active Control System of the California Extremely Large Telescope (CELT)," *SPIE* **4004**, 2000.
6. MacMartin, D. G., Mast, T. S., Chanan, G., and Nelson, J. E., "Active Control Issues for the California Extremely Large Telescope," *Guidance, Navigation, and Control Conference*, AIAA, 2001. AIAA 2001-4035.
7. Chanan, G., Troy, M., Dekens, F. G., Michaels, S., Nelson, J., Mast, T., and Kirkman, D., "Phasing the Mirror Segments of the Keck Telescopes: The Broadband Phasing Algorithm," *Applied Optics*, Vol. 37, pp. 140–155, 1998.
8. Cho, M. K., Stepp, L., and Kim, S., "Wind buffeting effects on the Gemini 8m primary mirrors," *SPIE* **4444**, *Optomechanical Design and Engineering*, 2001.
9. Padin, S., "Wind-induced Deformations in a Segmented Mirror," *Applied Optics*, Vol. 41, No. 13, pp. 2381–2389, 2002.